Nanoporous Multimetallic Ir Alloys As Efficient And Stable Electrocatalysts For Acidic Oxygen Evolution Reactions

Swarnendu Chatterjee[1], Saad Intikhab[1], Lauren Profitt[2], Yawei Li[1], Varun Natu[3], Ramchandra Gawas[1], Joshua Snyder[1,]*

[1]Department of Chemical and Biological Engineering, Drexel University, Philadelphia, PA 19104
[2]Department of Chemistry, Temple University, Philadelphia, PA 19122
[3]Department of Materials Science and Engineering, Drexel University, Philadelphia, PA 19104

*Corresponding author: Joshua Snyder, jds43@drexel.edu

Abstract

The dearth of appropriate electrocatalysts for stable anodic water splitting, oxygen evolution reaction (OER), in acid has given rise to concerted efforts toward making iridium-based high aspect ratio nanomaterials, as iridium and its higher valent oxides have been shown time and again to exhibit the most optimal balance between activity and durability. Here, we show a dealloying strategy to synthesize free-standing 3D oxide skinned nanoporous Ir electrocatalysts (np-Ir) with demonstrated enhanced activity and durability in comparison to more traditional IrO_x nanoparticulate catalysts. The metallic core and absence of any binder/support result in low electrode and charge transfer resistance, ultimately giving rise to lower OER overpotentials and improved activity.

1. Introduction

Water splitting through polymer electrolyte membrane (PEM) electrolysis is one of the more promising methods for renewable energy storage[1–4], storing renewably sourced energy[5–10] in the bonds of a hydrogen fuel[11,12]. The design of electrocatalysts for both anodic oxygen evolution (OER) and cathodic hydrogen evolution reactions (HER) is based on an appropriate

balance between activity, stability, and cost[13–16]. While alkaline water electrolysis benefits from low cost earth abundant electrode materials[17,18] e.g. oxides/hydroxides of Ni[19], Co[20], Mn[21], Fe[22] etc.; acidic electrolyzers, utilizing higher conductivity proton exchange ionomers/membranes, offer higher current densities and lower overpotentials. However, the corrosive pH of acidic PEM electrolyzers significantly limits the composition of viable OER electrocatalysts where the challenge remains overcoming kinetic barriers and poor chemical/structural stability in the severely oxidizing medium[23–25].

Early theoretical studies on the origin of OER overpotential for a number of metal oxides, revealed the kinetic barrier is defined by the scaling between HOO* and HO* binding energies on the catalyst surface[26,27]. A more recent work on IrO_2(110) single crystals shows these intermediates to be dependent on interactions between interfacial water and surface dipoles both of which are dependent on electrolyte composition and pH[28]. Oxides of Ru, Ir, and Pt sit at the peak of many computationally derived and experimentally validated volcano plots[26,27,29]. Of this group of transition metal oxides, RuO_x has been shown to exhibit the lowest OER overpotential yet it readily dissolves at operational potentials[30–32]. Thermal and electrochemical oxides of Ir, both amorphous and crystalline, while not as active as RuO_x, are considerably more stable than both RuO_x and PtO_x. This leaves IrO_x as one of the only viable electrocatalysts for acidic OER as it possess the most optimal balance of activity and stability among the transition metal oxides near the peak of the volcano[26,27]. The high cost and low minable quantity of Ir metal, however, has given rise to concerted efforts in reducing Ir content in PEM electrolyzer anode catalyst layers[33–35]. Two main strategies have emerged in the design of new Ir-based OER electrocatalysts: (1) development of unique high aspect ratio morphologies, such as nanoneedles[36], nanorods[37], nanodendrites[38], and oxide supported nanoparticles[39–

42], to maximize surface-to-volume ratio and increase mass-based activities[43–46] and (2) formation of Ir-transition metal alloys[33–35,38,43,47–50] to enhance the intrinsic activity of the Ir catalyst through electronic effects. Ni and Co have been the most commonly used metals to alloy with Ir, yielding improvements in intrinsic activity in comparison to IrO_x[33,35]. Other alloys reported include Ir – Fe[34], Cu[43], Mn[51], Te[49], W[47], and Cr[48]. In contrast to cathodic electrochemical reactions operating at lower absolute potentials[52,53], surface and near surface loss of the less stable transition metal alloying component readily occurs at OER relevant potentials[43,46,54–56]. This corrosive metal loss yields both Ir-shell nanostructures where the Ir surface possess a high density of defects active for OER[23,57] and porous/hollow nanostructures[46,56][55]. While many of these unique nanostructures and alloy compositions display high initial intrinsic activity, performance quickly decays under OER conditions due to compositional and morphological evolution. Metallic OER electrocatalysts convert to a nominal higher valent oxide at operational potentials, decreasing their intrinsic conductivity. The high density of oxide-oxide interfaces among the agglomerated nanoparticles within the catalyst layer adds additional resistivity to the catalyst layer. The overall result is a significant loss in performance at higher water oxidation rates due to the resistive losses[45,58], in addition to active area loss due to material corrosion. The rate of these processes increases as the length-scale of the material decreases.

Maintaining high activity for morphologically complex, high aspect ratio alloy nanostructures, which is a direct consequence of their high defect density and low average surface atom coordination[59,60], while mitigating losses associated with low in-plane and through-plane conductivity within the anode catalyst layer is not trivial. Moving beyond standard OER electrodes composed of agglomerated particles, free standing bicontinuous nanoporous metals offer many

advantages including their high surface-to-volume ratio, high defect density, negation of the need for carbon or oxide supports, and high intrinsic conductivity, both in-plane and through-plane, due to the interconnected metallic backbone of the nanoporous metal[44,45,52], see **Figure 1**. Nanoporous Ir can be formed through chemical/electrochemical dealloying of transition metal-rich Ir-transition metal alloys. However, in contrast to the dealloying of more noble metals such as Pt[60,61] and Au[62,63], Ir readily oxidizes under dealloying conditions which acts to slow curvature driven surface diffusion[64–66]. This will lead to surface passivation with immobile Ir and inhibit etch front propagation into the alloy. Strategies to mitigate this surface passivation include the use of a transition metal alloying component that forms a highly soluble oxide, such as Os[45]. The high rate of Os corrosion, potentially initiating Ir corrosion as well in the Os-rich alloy, prevents surface passivation and propagates porosity into the bulk of the alloy. Nanoporous Ir from Os-based alloys, however, exhibits feature sizes larger than 50 nm[45] and Os itself is a toxic and rare element. Reduction in the initial Ir content (< 5 at.%) in the parent alloy can lower the probability of surface passivation as the surface concentration of Ir is low. However, absent a sufficient percolation of Ir throughout the alloy, the evolved nanostructure following dealloying lacks any structural integrity[44].

In this work we present a strategy to drive the formation of free standing nanoporous Ir through electrochemical dealloying. We show that optimization of the precursor alloy and electrolyte compositions can prevent surface passivation with immobile Ir species and yield bicontinuous porosity, all internal surface area is accessible from the exterior of the nanoporous material[62,67], with length scales below 10 nm. The free-standing nanoporous Ir electrodes, requiring no ionomer or polymeric binder to form a catalytic electrode, exhibit a low intrinsic resistivity and higher intrinsic OER activity in comparison to an IrO_x agglomerated nanoparticle

electrode. A distinct advantage of dealloying is the ability to incorporate additional metallic components through the use of multi-metallic precursor alloys[63,68]. We show that a ternary element, Cr, is facilely added to the nanoporous structure through metallurgical incorporation into the precursor alloy. However, in contrast to previous reports[48], no statistically relevant increase in OER activity is observed. Regardless, the high OER activity and enhanced in-plane and through-plane conductivity of free-standing nanoporous metal electrodes represents a new class of electrocatalysts with potential for integration into commercial PEM water electrolyzers.

2. Experimental

2.1 Catalyst preparation

Nanoporous iridium alloys (np-Ir) are prepared by electrochemical dealloying of different compositions of Ni_xIr_y, $Ni_xIr_yCr_z$, Cu_xIr_y, Ag_xIr_y and Co_xIr_y ($x \geq 80$; $y \leq 20$; $z \leq 5$ at.%) alloy foils. Following melting and homogenization of the alloys from high purity precursor metals (Ni, Co, Ag and Cu pellets from Kurt J Lesker, purity above 99.9%; Ir pellets from Goodfellow, purity 99.9%; and Chromium from Alfa Aesar, purity 99.995%) in a radio frequency induction furnace (Ambrell EasyHeat 3542 LI) under Ar gas, the alloys are rolled into thin ribbons using a rolling mill. Intermittent annealing under Ar is used during the rolling process to remove work hardening and promote homogenization of the precursor alloys.

As a consequence of the strong composition dependence of dealloying rates, dealloying conditions are optimized for each of the different alloys. np-Ir and np-IrCr are prepared by electrochemically dealloying (three electrode cell with Toray carbon paper counter electrode and Ag/AgCl (BASi) reference electrode) Ni-Ir and Ni-Ir-Cr alloys in 100 mM HCl + 1 M H_2SO_4 with potential cycling between −0.05 and 1 V vs. RHE at a scan rate of 50 mV/s (100 cycles) (further

details provided in supplementary information). np-Ir from Cu-Ir alloys is prepared by dealloying $Cu_{85}Ir_{15}$ in 0.1 M H_2SO_4 with potential cycling between -0.05 and 1 V vs. RHE (100 cycles). np-Ir from Ag-Ir alloys is prepared by dealloying $Ag_{85}Ir_{15}$ in 0.1 M HNO_3 with potential cycling between 0.35 and 1.3 V vs. RHE (100 cycles). np-Ir from Co-Ir alloys is prepared by dealloying $Co_{95}Ir_5$ in 100 mM HCl + 1 M H_2SO_4 with potential cycling between -0.05 and 1 V vs. RHE (100 cycles) The nanoporous electrodes are rested in Millipore water (Milli-Q synthesis A10) following dealloying to remove any residual acid and transition metal ions within the pores.

IrO_x nanoparticles are used as the control catalyst; ink of Iridium (IV) oxide nanoparticles (Alfa Aesar, purity 99.9 %) is prepared in 2-propanol (Sigma-Aldrich, assay: 99.999%) aqueous solution (isopropanol:water = 1:4) (10 mg/ml) with nafion solution (Ion Power) (10 µl 5 wt.% nafion solution in 1 ml ink) as a binder. The catalyst ink is drop cast on Ti foil (0.325±0.02 cm^2) precleaned in boiling oxalic acid (10% w/v, Beantown Chemical) with an approximate electrocatalyst loading of 0.2 mg/cm^2.

2.2 Material characterization

The structure, morphology and elemental composition of Ir electrocatalysts are analyzed using transmission electron microscopy (TEM) (JEOL JEM2100), scanning TEM (STEM), energy dispersive X-Ray spectroscopy (EDS) (JEOL 2100F), and scanning electron microscopy (SEM) (Zeiss Supra 50VP). Selected area electron diffraction (SAED) and high resolution TEM (HRTEM) have been used to confirm crystallinity of the nanoporous Ir alloys. X-ray diffraction (XRD) spectra for phase purity of precursor alloys of Ni-Ir and Ni-Ir-Cr are analyzed on a Rigaku SmartLab diffractometer with a Cu Kα X-ray source operated at 40 kV and 30 mA. To quantify dissolution of metals during durability analysis, the electrolyte is analyzed with inductively coupled plasma optical emission spectrometry (ICP-OES) on an iCAP 7000 Series Spectrometer

(Thermo Scientific) functioning in axial mode with a reference power of 1150 W, auxiliary and nebulizer gas flows of 0.5 L/min, and a pump speed of 50 rpm. A Physical Electronics VersaProbe 5000 (Physical Electronics, Chanhassen, Minnesota, USA) instrument is used to obtain high-resolution X-ray photoelectron spectroscopy (XPS) spectra. Monochromatic Al-Kα X-rays with the spot size of 200 μm is used to irradiate the sample surface. Pass energy of 23.5 eV, with a step size of 0.5 eV is used to gather the high-resolution spectra. CasaXPS Version 2.3.19PR1.0 software is used for peak fitting. The XPS spectra are calibrated by setting the valence edge to zero, which is calculated by fitting the valence edge with a step-down function and setting the intersection to 0 eV. The background is determined using the Shirley algorithm, which is a built-in function in the CasaXPS software. Because Ir and Ir oxides are conductive in nature its peaks are fit using an asymmetric line function[69].

2.3 Electrochemical measurements

All the electrochemical experiments are conducted in a three-electrode electrochemical cell using an Autolab PGSTAT128N potentiostat. The OER is performed in Ar-purged 0.1 M $HClO_4$ (OmniTrace Ultra, Millipore) made with Millipore water. An Ag/AgCl electrode (BASi) is used as the reference electrode with Toray carbon paper as the counter electrode. The electrolyte is stirred at 1000 rpm during recording of OER polarization curves. All the glassware is cleaned in a 1:1 v:v solution of concentrated sulfuric and nitric acids followed by boiling in Millipore water before each use. Electrochemical impedance spectroscopy (EIS) is used to measure ohmic and charge transfer resistances of the Ir electrocatalysts at onset and kinetically active OER relevant potentials (1.44 V and 1.51 V vs. RHE respectively). A frequency range of 10 mHz to 100 KHz has been used with an amplitude of 10 mV. All the EIS data for different electrocatalysts are normalized by geometric area of the electrode.

3. Results and Discussion

Nanoporosity evolution through electrochemical dealloying is limited by strict precursor material requirements, most notably the formation of a homogeneous solid solution or ordered intermetallic, a sufficient percolation of the less noble alloying component, and sufficient separation in the redox potentials of the alloy components[45,62,63]. Movement of the etch front into the bulk of the material is predicated on the dissolution of the less noble component and sufficient rates of surface diffusion of the remaining more noble component. Slow rates of diffusive movement of the remaining more noble component yield smaller pores sizes, due to the higher density of pore bifurcation events[63,70,71]. However, this slow diffusive movement of the more noble component can also lead to surface passivation, preventing the movement of the etch front into the material and stymying the evolution of nanoporosity. The magnitudes of surface diffusivity coefficients for metals scale roughly with melting point[66,72]. For Ir, possessing a higher melting point than both Au and Pt, and consequently a lower surface diffusivity, the reduced onset potential for oxide formation yields an additional challenge to nanoporosity evolution. Specifically, the lower nobility compared to Pt and Au results in a facile surface passivation with an immobile oxide species, increasing the barrier for etch front propagation into the bulk of the metal. In **Figure 2(a)**, traditional dealloying in 1 M H_2SO_4 by potential cycling for an IrNi alloy yields a surface that is absent of any porosity. This is in contrast to what was observed previously with IrOs alloys, where large scale porosity was evolved[45]. The case of IrOs dealloying is particularly unique in that the high rate of Os corrosion, in part due to the high aqueous solubility of its high valent species, acts to unintentionally remove Ir from the surface as well[45]. This circumvents the slow rate of surface reorganization for Ir. IrNi, however, is a much more practical precursor alloy due to the ready formation of a homogeneous solid solution through standard

metallurgical methodologies, relatively low cost and minimal toxicity of Ni. It is also possible to recover the Ni through electrodeposition from solution.

Propagation of the etch front into an IrNi surface, even in the limit of low Ir content (< 20 at.% Ir), requires the fast corrosion of Ni followed by rapid rearrangement of the exposed, lower coordination Ir. The addition of Cl^- to the dealloying electrolyte increases the oxidizing power of the electrolyte. In **Figure 2(b)**, it is shown that the addition of ~ 100 mM Cl^- to the 1 M H_2SO_4 electrolyte yields a distributed and homogeneous nanoporous morphology following potentiodynamic dealloying. The Cl^- ions in solution result in: (1) an increase in the local solubility of Ni at the etch front, promoting its fast dissolution, (2) an increase in the rate of Ir surface diffusion, which would act to facilitate exposure of underlying Ni within the alloy, through the complexing of surface Ir atoms, promoting their mobility[73–76], and (3) promotion of the limited dissolution of Ir which would negate the impact of both slow moving Ir and surface oxide passivation on Ni dissolution and etch front propagation. Further evidence of the impact of native surface oxides is shown in the contrasting structural evolution of Ir alloys following potentiostatic and potentiodynamic dealloying. During constant potential holds at 1 V vs. RHE in 1 M H_2SO_4, current decay (**Figure S2(a)**) with time suggests the cessation of etch front propagation. No porosity formation is observed at 1 V vs. RHE in 1 M H_2SO_4, **Figure S2(b)**, in the absence of Cl^-. However, when 100 mM HCl is added to the electrolyte, the current transient increases with time, **Figure S2(a)**. This is characteristic of etch front propagation into the alloy and nanoporosity evolution[77]. The presence of Cl^- ions, either by enhanced Ni dissolution, inhibition of Ir oxide formation, enhanced surface diffusion of remaining Ir atoms or dissolution of high valent Ir species, creates a functional nanoporosity on the surface. The rate of porosity evolution/etch front propagation, however, remains low for potentiostatic dealloying as surface oxidation of Ir at these

high potentials remains possible. Contrasting this with potentiodynamic dealloying, following 100 cycles between -0.05 V and 1.0 V in 1 M H_2SO_4 + 100 mM HCl a bicontinuous nanoporosity evolves[45,52,63], **Figure 2(b)**. The higher rate of etch front propagation during potential cycling is a consequence of the reduction of surface oxides during the cathodic sweep, facilitating atomic reorganization and exposure of underlying Ni for continued etching.

In **Figures S3 and S4** we assess the sensitivity of porosity evolution to the precursor alloy composition, in terms of the identity of the less noble component (Ni, Cu, Ag, Co) and the total fraction of less noble component in the alloy. We find that np-Ir is readily evolved at Ni contents greater than 80 at.%, **Figure S3**. While this is likely not the lower bound of the compositional parting limit range, we find below 80 at.%, dealloying currents greatly diminish. This is likely due to a critical concentration of slow moving Ir/IrO_x that acts to partially passivate the surface. Of the higher Ni content alloys tested, we find np-Ir formed from the potentiodynamic dealloying of a precursor alloy containing 85 at.% Ni to give an even, homogeneous porosity over large areas of the foil electrode, **Figure 2(b) and S3(b)**, with pore sizes ranging between 5 and 10 nm. Synthesis of np-Ir is also assessed using Ag, Co, and Cu as the sacrificial alloying component. Dealloying of $Ag_{85}Ir_{15}$ and $Co_{95}Ir_5$ yield nanoporous structures with large, irregular porosity, **Figure S4(b) and (c)**. This is a consequence of the poor mixing and phase separation as CoIr has a large miscibility gap at low Ir contents and AgIr phase separates at all compositions[78]. In contrast, the dealloying of $Cu_{85}Ir_{15}$ yields a homogeneous morphology, similar to that for $Ni_{85}Ir_{15}$, **Figure S4(a)**. However, following the initial movement of the etch front into the alloy, the high rate of Cu dissolution, which is a consequence of its nobility and inability to form a stable passive oxide, results in rapid dealloying of the entire alloy foil. The brittle nature of the completely dealloyed

foil causes it to break apart, making it difficult to form freestanding electrodes like those shown in **Figure S1(c)**.

The distinct advantage that top-down synthesis methodologies such as dealloying have over other techniques is the ability to readily incorporate multiple metallic species, multi-component alloys, which end up homogeneously distributed throughout the entire nanostructure[63,68]. The incorporation of ternary and even quaternary components allows one to tune the functional properties of the material. Altering the electronic structure of the surface atoms in nanoporous alloys for favorable binding energies of reaction intermediates is a well-established technique for a number of catalytic reactions[52,79,80]. In a recent work[48], incorporation of 20 at.% Cr into a rutile IrO_2, in the form of a homogeneous dispersion of the dopant metal throughout the oxide, was theoretically and experimentally shown to reduce the OER overpotential in comparison to pure IrO_2. Catalysis on homogeneous surface alloys is dictated by both altered electronic properties of the primary catalytic entity, high valent Ir, and the additional active sites provided by the alloying component. For segregated core-shell structures, the secondary alloying component remains beneath the active surface. However, it induces a shift in the electronic properties of the surface atoms, affecting thermodynamics and kinetics of the reaction[48,52,81]. With the facile introduction of additional metals into the nanoporous catalyst through physical metallurgy and dealloying, i.e. Cr, we can assess the impact of ternary components on OER activity. Foils of $Ni_{85}Ir_{10}Cr_5$ are prepared through RF melting/homogenization and dealloying using the above-mentioned dealloying protocols. TEMs shown in **Figure 3** confirm a uniform bicontinuous porosity that extends into the bulk of the alloy for both np-Ir and np-IrCr. The selected area electron diffraction (SAED) analysis, **Figure 3(a)** and **(b)** insets, and high resolution TEM (HRTEM), **Figure 4(a)**, of np-Ir and np-IrCr highlight the crystalline nature of the

nanostructures with a prominent fcc (111) orientation (0.22 nm) visible. As a consequence of the layer-by-layer mechanism of dealloying and etch front propagation, the surfaces of the np-Ir/np-IrCr ligaments are passivated with Ir while some fraction of the alloying components, Cr and/or Ni in this case, remain in the interior of the ligaments. Energy Dispersive X-Ray spectroscopy (EDS) mapping of elements in Scanning Transmission Electron Microscopy (STEM) mode, **Figure 4(b)**, of the np-IrCr obtained from dealloying $Ni_{85}Ir_{10}Cr_5$ reveals that the nanoporous metal is mostly Ir, with small amounts of Ni and Cr remaining (Ni ~ 4.8 at% and Cr ~ 1.8 at%). X-Ray Photoelectron spectroscopy (XPS) analysis, **Figure 5**, of the as-dealloyed np-Ir and np-IrCr indicates that the surface is covered by IrO_x ($0 < x < 2$) as only one pair of peaks at 61.2 eV (Ir $4f_{7/2}$) and 64.2 eV (Ir $4f_{5/2}$) is observed in the Ir high resolution spectra. This corresponds to mostly Ir^{4+} oxidation state[69,82]. However, it is also important to note regardless of the initial surface valence state of Ir, it slowly transforms to a higher valence state than +4 at OER relevant potentials[23,82]. For both dealloyed compositions, the signals for Ni and Cr are low. This is an indication that little Ni or Cr remain near the surface of the catalyst. This is a consequence of the mechanism of nanoporosity evolution through dealloying and suggests that any electronic impacts on the OER activity may be minimal.

Prior to OER testing, all np-Ir electrodes are subjected to a 24 hour chronoamperometric potential hold at 1.51 V, the goal being to a structure and composition that is at a relative steady state, remaining unchanged during OER polarization curves, **Figure S6**. ICP-OES analysis of the electrolyte (**Table S1**) following the potential hold indicates that Ni dissolution contributed to 9-11% of the charge passed, while that for Cr accounted for < 0.5%. It is found that the Ir dissolution current during the potential hold remains negligible (0.01 – 0.02 %). The OER performance of np-Ir and np-IrCr are compared to that of IrO_x nanoparticles in 0.1 M $HClO_4$, **Figure 6**. For these half-

cell tests, the np-Ir and np-IrCr are free standing electrodes whereas the IrO_x nanoparticles are deposited on Ti foil with Nafion as an ionomeric binder. For removal of bubbles and any O_2 concentration gradients established during OER, the electrolyte is stirred (stirring rate: 1000 rpm). The iR corrected OER polarization curves are obtained by sweeping the potential 0.5 V and 1.6 V vs. RHE at 10 mV/s. As shown in **Figure 6(a)**, the OER onset potentials for np-Ir and IrO_x nanoparticles are approximately 1.4 V vs. RHE, as expected for Ir oxides[30,45,48] whereas that of np-IrCr is approximately 1.35 V vs. RHE. Normalizing by the geometric area of the electrodes, the measured overpotential at 10 mA/cm^2 for IrO_x is found to be 331 ± 13 mV whereas that for np-Ir and np-IrCr are found to be substantially lower at 259 ± 4 mV and 252 ± 3 mV respectively, **Figure 6(c)**. Comparing the true intrinsic activity amongst compositionally and morphologically varied electrocatalysts requires analysis of the electrochemically active surface area (ECSA). There remains controversy, particularly for OER catalysts that possess a hydrous oxide on the surface, as to the most accurate methodology for determining ECSA. The two most common techniques for calculating ECSA are the Brunauer–Emmett–Teller (BET) method and non-faradaic double layer capacitance (C_{dl})[45,83,84]. While the BET method is applicable for nanomaterials that can be obtained in powder form[83,84], it is particularly challenging for nanoporous metals in a foil geometry, as is used here. Here we willfully acknowledge the significant limitations of the C_{dl} methodology for determining ECSA and roughness factors of transition metal oxide OER electrocatalysts. The most significant limitation is the convolution of the contributions to the measured double layer current. In addition to the non-faradaic charging, faradaic processes including ion intercalation through the hydrous oxide layer, H^+/OH^- and other ion specific adsorption, corrosion, etc.[85–88], contribute to the measured current. Additionally, resistivity of the electrode material has been demonstrated to have a significant impact on the

discrepancy between the surface area measured by BET and that determined by C_{dl}, with the difference increasing with a decrease in electrode conductivity [83,88]. Limitations to C_{dl} based ECSA measurements for Ir-oxides, in addition to the difficulty in identifying the potential region associated with true non-faradaic capacitive charging on the oxophilic Ir surface, and possible interference of electrolyte ions or any residual charge transfer processes[83,84,89], include the absence of any universal specific capacitance value of "flat" Ir-oxide. Based on these limitations, analysis of ECSA normalized activity is good only to gain comparative insights within a set of samples tested with similar protocols. In previous works, a range of specific capacitance values have been used for ECSA determination of IrO_x electrocatalysts[51,90,91]. For example, Chen and co-workers[91] have calculated a specific capacitance of 0.65 mF/cm^2 from a previous report of single crystal IrO_2(100)[92]. On the other hand, Jaramillo and co-workers[90] have assumed a statistical average specific capacitance value of 0.035 mF/cm^2 for normalization of a number of OER electrocatalysts including IrO_x. Here, we have followed the work of Chen and co-workers[91] for determination of ECSA (roughness factor) based on the double layer capacitive current densities at 0.45 V vs. RHE in 0.5 M H_2SO_4 obtained through cyclic voltammograms at different scan rates, **Figures S7** and **S8**. We acknowledge the potential error in using this methodology of ECSA determination but will use it here only for comparative purposes. Comparing the average ECSA normalized OER current densities at 1.51 V vs. RHE as measured by constant potential electrolysis over a period of 24 hours, **Figure S8**, demonstrates the high intrinsic activity of both np-Ir and np-IrCr (194 - 218 μA/cm^2) compared to that of IrO_x (84 - 92 μA/cm^2). Overall, the self-supported np-Ir and np-IrCr electrodes display low overpotentials and high durability during low pH constant potential electrolysis when compared to IrO_x, **Figures 6(b)** and **S9**. Additionally, the nanoporous catalyst developed here compares favorably to other Ir and Ir alloy based

nanocatalysts, **Table S2**. Taken together, the OER polarization overpotential, **Figure 6(c)**, and the ECSA normalized electrolysis current density, **Figure S8**, for np-Ir and np-IrCr indicate that in the current catalyst form and method of preparation, the addition of Cr results in a negligible impact to the intrinsic activity of the catalyst. This is most likely due to the electrochemical corrosion of surface and near surface Cr both during dealloying and OER. The apparent early OER onset on np-IrCr in comparison to np-Ir is likely a consequence of the impact of the Cr additive on the hydrous oxide formation on the nanoporous structure as indicated by the significant increase in the sweep rate dependent pseudocapacitive and faradaic currents on np-IrCr as compared to np-Ir.

An overlooked but unique property of nanoporous metals, that offers a distinct advantage for OER catalysts, is the interconnectivity of the nanostructures in the electrode. Nanoporous metals have bicontinuous nanoporosity which means that all open volume within the bulk of the nanostructure is accessible from the exterior of the monolith. This also means that there is a continuous metallic backbone running throughout the architecture which provides an uninterrupted pathway for electrons to travel. In contrast, traditional OER electrodes are composed of agglomerated oxide particles held together by a polymeric ionomer and exhibit high in-plane and through-plane resistivity[93–96], see **Figure 1**. The overall performance and energy consumption of an OER electrode is defined by the resistance to charge transfer for the reaction and the overall conductivity of the electrode, where the latter is dictated by both carrier mobility and carrier density[45]. In order to make direct comparisons between the bicontinuous nanoporous electrodes and those composed of agglomerated nanoparticles, it is crucial to understand how carrier mobility and density differ in these two distinct catalyst microstructures. As observed in the Ir-Os system[45], the carrier density values are similar to those for agglomerated IrO_2 nanoparticles. However, the carrier mobility in nanoporous Ir is several times higher than that in agglomerated

IrO_2 nanoparticles[45]. The high mobility in the former is a result of the presence of a metallic backbone below a few nm thick IrO_x layer on the surface. The uninterrupted path for electrons to move in nanoporous metals is contrasted with that for agglomerated Ir oxide particle electrodes which are characterized by a high density of oxide-oxide interfaces, **Figure 1**. The polymeric ionomer binder in agglomerated electrodes also inhibits electron movement in-plane and through-plane. The free-standing np-Ir and np-IrCr electrodes developed here do not require ionomeric binder for half-cell testing.

Here, electrochemical impedance spectroscopy (EIS) is carried out in the frequency range of 10 mHz to 100 KHz (amplitude 10 mV) to assess the variability in the ohmic resistances which can be correlated to the electrode resistivity. EIS spectra are analyzed using the equivalent Randles circuit[97] suitable for heterogeneous electrochemical systems, **Figure 7**, where the diameter of the semicircle denotes the charge transfer resistance and the starting point of the semicircle denotes the total ohmic resistance. The ohmic resistance constitutes the series combination of resistances in the external circuit (wires and other connections), electrode internal resistance and the solution resistance[84,89,97]. The solution resistance is dependent on the ion concentration of the electrolyte, rate of bubble removal from catalyst surface and the distance between the working (WE) and reference electrode (RE)[89,97]. In our experiments, we have performed the EIS analysis at a constant electrolyte composition (0.1 M $HClO_4$), fixed stirring rate to ensure minimal interference of bubbles, and a constant distance of ~ 2.5 cm between the WE and RE (It has been shown that within a distance of around 4-5 cm, small changes in distance between the WE and RE do not alter the ohmic resistance substantially[89]). We have measured the ohmic resistances (R_{ohmic}) and the charge transfer resistances at two potentials, one just above the OER onset potential, 1.44 V (R_{ct}^{onset}) and another at 1.51 V (R_{ct}). For iridium based OER electrocatalysis, a

wide range of R_{ohmic} values have been reported[37,91,93,97–99] as a consequence of the variance in catalyst morphology composition, supports, electrolyte composition, electrochemical setup, and supporting electrode. As an example, different R_{ohmic}, R_{ct}^{onset}, and R_{ct} values are obtained for IrO_x loaded on a glassy carbon (GC) or a Ti foil (GC: R_{ohmic} = 8 **Ω** cm^2, R_{ct}^{onset} = 292 **Ω** cm^2, and R_{ct} = 24 **Ω** cm^2; Ti foil: R_{ohmic} = 6 **Ω** cm^2, R_{ct}^{onset} = 92 **Ω** cm^2, and R_{ct} = 13 **Ω** cm^2), **Figure S10**. While deconvolution of contributions from external circuit resistance, electrode internal resistance, and solution resistance is difficult, comparing the R_{ohmic} values of IrO_x supported on Ti foil with that of np-Ir and np-IrCr foil electrodes under identical electrolyte and reaction conditions (distance between WE and RE, stirring rate, pressure and temperature (293 ± 3 °K)) can provide qualitative insights on the difference between electrode internal resistances. **Figure 7** contains the Nyquist plots for np-Ir, np-IrCr, and Ti supported IrO_x at 1.44 V and 1.51 V vs. RHE. The resistance values are summarized in **Table S3**. For the nanoporous electrodes, the R_{ohmic} lies between 3.4 – 3.5 **Ω**.cm^2 which is significantly less than that of IrO_x, ~ 6 **Ω** cm^2, and other nanostructured Ir/IrO_x OER electrocatalysts[98]. Additionally, IrO_x exhibits higher charge transfer resistances both at 1.44 V (R_{ct}^{onset} ~ 92 **Ω** cm^2) and at 1.51 V (R_{ct} ~ 13 **Ω** cm^2). The R_{ct}^{onset} and R_{ct} of np-Ir are 84.85 ± 2.19 **Ω** cm^2 and 3.76 ± 0.34 **Ω** cm^2, while those of np-IrCr are 55.19 ± 1.71 **Ω** cm^2 and 3.61 ± 0.27 **Ω** cm^2, respectively. The lower R_{ct}^{onset} for np-IrCr compared to that of np-Ir is likely a result of the impact of Cr on the formation and stoichiometry of the hydrous oxide formed on the surface of Ir at OER relevant potentials, **Figure S7**. As the kinetic activity is a function of both interfacial charge transfer and total system ohmic resistance, at least a part of the performance enhancement for np-Ir and np-IrCr over IrO_x nanoparticles can be attributed to the significant reduction in electrode resistivity. This demonstrates the significant advantage of the interconnected nanoporous metal electrodes, potentially resulting in improved electrolyzer high current density performance.

The durability of the nanoporous electrodes is assessed through extended (24 hours) electrolysis at 1.51 V RHE. For both np-Ir and np-IrCr the specific current densities do not show any significant decay, **Figure 6(b)**. In contrast, the IrO_x electrode shows continued decay during constant potential electrolysis, **Figure S11.** The current decay can be attributed to a range of issues including change in Ir oxidation state and nanoparticle migration/coalescence or detachment[58,93,100]. Following extended electrolysis, SEM analysis of the nanoporous electrodes indicates minimal change to the electrode morphology, **Figure S12**. The dissolution of metals into the electrolyte during constant potential electrolysis is analyzed by ICP-OES. Ni dissolution contributes to 2.4% of the total charge passed for np-Ir and 1.9 % for np-IrCr. Little loss in Cr or Ir is observed, accounting for only 0.15 % and < 0.01 % of the charge passed, respectively. The nanoporous Ir electrodes are active and stable electrocatalysts for extended OER during electrolysis characterized by a high intrinsic area, interconnected morphology and low electrode resistivity.

4. Conclusion

In summary, we have demonstrated a modified dealloying protocol to make free standing 3D bicontinuous nanoporous alloys of IrNi (np-Ir) which demonstrate enhanced activity (251 – 259 mV overpotential at 10 mA/cm^2_{geo}) and durability for acidic OER electrolysis compared to a nanoparticulate IrO_x catalyst. The nanoporous Ir electrocatalysts exhibit high intrinsic activity, arising from the high roughness factor (>50) coupled with a low in-plane and through-plane resistivity, and morphological stability for sustained electrolysis (>24 hours). The intrinsic activity, normalized by the real ECSA, for both np-Ir and np-IrCr is found to greatly exceed that of IrO_x. This is attributed to the unique atomic morphology of the high aspect ratio nanoporous metals and

the interconnected metallic back bone that leads to high in-plane and through-plane conductivity and reduced ohmic and charge transfer resistances. The addition of a ternary alloying component, Cr, is facile through physical metallurgical methods followed by dealloying. However, no impact of the Cr on the intrinsic activity of the nanoporous Ir is observed. This is likely due to the removal of surface and near surface Cr during dealloying or time spent at OER relevant potentials. The performance of the np-Ir electrodes presented here demonstrates their promise to overcome present bottlenecks in acidic OER electrocatalysis.

Acknowledgements

We gratefully acknowledge support from the ACS-PRF (57565-DNI5) and NSF-DMR 1904571.

References:

[1] P. Millet, R. Ngameni, S.A. Grigoriev, N. Mbemba, F. Brisset, A. Ranjbari, C. Etiévant, PEM water electrolyzers: From electrocatalysis to stack development, Int. J. Hydrogen Energy. 35 (2010) 5043–5052. https://doi.org/10.1016/j.ijhydene.2009.09.015.

[2] E. Slavcheva, I. Radev, S. Bliznakov, G. Topalov, P. Andreev, E. Budevski, Sputtered iridium oxide films as electrocatalysts for water splitting via PEM electrolysis, Electrochim. Acta. 52 (2007) 3889–3894. https://doi.org/10.1016/j.electacta.2006.11.005.

[3] P. Millet, N. Mbemba, S.A. Grigoriev, V.N. Fateev, A. Aukauloo, C. Etiévant, Electrochemical performances of PEM water electrolysis cells and perspectives, Int. J. Hydrogen Energy. 36 (2011) 4134–4142. https://doi.org/10.1016/j.ijhydene.2010.06.105.

[4] S. Siracusano, A. Di Blasi, V. Baglio, G. Brunaccini, N. Briguglio, A. Stassi, R. Ornelas, E. Trifoni, V. Antonucci, A.S. Aricò, Optimization of components and assembling in a PEM electrolyzer stack, Int. J. Hydrogen Energy. 36 (2011) 3333–3339.

https://doi.org/10.1016/j.ijhydene.2010.12.044.

[5] M.G. Walter, E.L. Warren, J.R. McKone, S.W. Boettcher, Q. Mi, E.A. Santori, N.S. Lewis, Solar Water Splitting Cells, Chem. Rev. 110 (2010) 6446–6473. https://doi.org/10.1021/cr1002326.

[6] J.R. McKone, N.S. Lewis, H.B. Gray, Will Solar-Driven Water-Splitting Devices See the Light of Day?, Chem. Mater. 26 (2014) 407–414. https://doi.org/10.1021/cm4021518.

[7] A. Landman, H. Dotan, G.E. Shter, M. Wullenkord, A. Houaijia, A. Maljusch, G.S. Grader, A. Rothschild, Photoelectrochemical water splitting in separate oxygen and hydrogen cells, Nat. Mater. 16 (2017) 646–651. https://doi.org/10.1038/nmat4876.

[8] J. Jia, L.C. Seitz, J.D. Benck, Y. Huo, Y. Chen, J.W.D. Ng, T. Bilir, J.S. Harris, T.F. Jaramillo, Solar water splitting by photovoltaic-electrolysis with a solar-to-hydrogen efficiency over 30%, Nat. Commun. 7 (2016) 13237. https://doi.org/10.1038/ncomms13237.

[9] P. Ahmadi, I. Dincer, M.A. Rosen, Energy and exergy analyses of hydrogen production via solar-boosted ocean thermal energy conversion and PEM electrolysis, Int. J. Hydrogen Energy. 38 (2013) 1795–1805. https://doi.org/10.1016/j.ijhydene.2012.11.025.

[10] G. Peharz, F. Dimroth, U. Wittstadt, Solar hydrogen production by water splitting with a conversion efficiency of 18%, Int. J. Hydrogen Energy. 32 (2007) 3248–3252. https://doi.org/10.1016/j.ijhydene.2007.04.036.

[11] F. Barbir, PEM electrolysis for production of hydrogen from renewable energy sources, Sol. Energy. 78 (2005) 661–669. https://doi.org/10.1016/j.solener.2004.09.003.

[12] S. Intikhab, V. Natu, J. Li, Y. Li, Q. Tao, J. Rosen, M.W. Barsoum, J. Snyder, Stoichiometry and surface structure dependence of hydrogen evolution reaction activity

and stability of MoxC MXenes, J. Catal. 371 (2019) 325–332. https://doi.org/10.1016/j.jcat.2019.01.037.

[13] F. Dionigi, T. Reier, Z. Pawolek, M. Gliech, P. Strasser, Design Criteria, Operating Conditions, and Nickel-Iron Hydroxide Catalyst Materials for Selective Seawater Electrolysis, ChemSusChem. (2016). https://doi.org/10.1002/cssc.201501581.

[14] N.-T. Suen, S.-F. Hung, Q. Quan, N. Zhang, Y.-J. Xu, H.M. Chen, Electrocatalysis for the oxygen evolution reaction: recent development and future perspectives, Chem. Soc. Rev. 46 (2017) 337–365. https://doi.org/10.1039/C6CS00328A.

[15] Y. Jiao, Y. Zheng, M. Jaroniec, S.Z. Qiao, Design of electrocatalysts for oxygen- and hydrogen-involving energy conversion reactions, Chem. Soc. Rev. 44 (2015) 2060–2086. https://doi.org/10.1039/C4CS00470A.

[16] V.R. Stamenkovic, D. Strmcnik, P.P. Lopes, N.M. Markovic, Energy and fuels from electrochemical interfaces, Nat. Mater. 16 (2017) 57–69. https://doi.org/10.1038/nmat4738.

[17] I. Roger, M.A. Shipman, M.D. Symes, Earth-abundant catalysts for electrochemical and photoelectrochemical water splitting, Nat. Rev. Chem. 1 (2017) 0003. https://doi.org/10.1038/s41570-016-0003.

[18] J. Li, G. Zheng, One-Dimensional Earth-Abundant Nanomaterials for Water-Splitting Electrocatalysts, Adv. Sci. 4 (2017) 1600380. https://doi.org/10.1002/advs.201600380.

[19] P.W.T. Lu, Nickel-Based Alloys as Electrocatalysts for Oxygen Evolution from Alkaline Solutions, J. Electrochem. Soc. 125 (1978) 265. https://doi.org/10.1149/1.2131426.

[20] J. Chen, C. Fan, X. Hu, C. Wang, Z. Huang, G. Fu, J. Lee, Y. Tang, Hierarchically Porous Co/Co x M y (M = P, N) as an Efficient Mott–Schottky Electrocatalyst for Oxygen

Evolution in Rechargeable Zn–Air Batteries, Small. 15 (2019) 1901518. https://doi.org/10.1002/smll.201901518.

[21] X. Xiong, Y. Ji, M. Xie, C. You, L. Yang, Z. Liu, A.M. Asiri, X. Sun, MnO2-CoP3 nanowires array: An efficient electrocatalyst for alkaline oxygen evolution reaction with enhanced activity, Electrochem. Commun. 86 (2018) 161–165. https://doi.org/10.1016/j.elecom.2017.12.008.

[22] F.J. Pérez-Alonso, C. Adán, S. Rojas, M.A. Peña, J.L.G. Fierro, Ni/Fe electrodes prepared by electrodeposition method over different substrates for oxygen evolution reaction in alkaline medium, Int. J. Hydrogen Energy. 39 (2014) 5204–5212. https://doi.org/10.1016/j.ijhydene.2013.12.186.

[23] N. Danilovic, R. Subbaraman, K.C. Chang, S.H. Chang, Y.J. Kang, J. Snyder, A.P. Paulikas, D. Strmcnik, Y.T. Kim, D. Myers, V.R. Stamenkovic, N.M. Markovic, Activity-stability trends for the oxygen evolution reaction on monometallic oxides in acidic environments, J. Phys. Chem. Lett. 5 (2014) 2474–2478. https://doi.org/10.1021/jz501061n.

[24] S.H. Chang, J.G. Connell, N. Danilovic, R. Subbaraman, K.-C. Chang, V.R. Stamenkovic, N.M. Markovic, Activity–stability relationship in the surface electrochemistry of the oxygen evolution reaction, Faraday Discuss. 176 (2014) 125–133. https://doi.org/10.1039/C4FD00134F.

[25] D.Y. Chung, P.P. Lopes, P. Farinazzo Bergamo Dias Martins, H. He, T. Kawaguchi, P. Zapol, H. You, D. Tripkovic, D. Strmcnik, Y. Zhu, S. Seifert, S. Lee, V.R. Stamenkovic, N.M. Markovic, Dynamic stability of active sites in hydr(oxy)oxides for the oxygen evolution reaction, Nat. Energy. (2020). https://doi.org/10.1038/s41560-020-0576-y.

[26] J. Rossmeisl, Z.-W. Qu, H. Zhu, G.-J. Kroes, J.K. Nørskov, Electrolysis of water on oxide surfaces, J. Electroanal. Chem. 607 (2007) 83–89. https://doi.org/10.1016/j.jelechem.2006.11.008.

[27] J. Rossmeisl, A. Logadottir, J.K. Nørskov, Electrolysis of water on (oxidized) metal surfaces, Chem. Phys. 319 (2005) 178–184. https://doi.org/10.1016/j.chemphys.2005.05.038.

[28] D.-Y. Kuo, J.K. Kawasaki, J.N. Nelson, J. Kloppenburg, G. Hautier, K.M. Shen, D.G. Schlom, J. Suntivich, Influence of Surface Adsorption on the Oxygen Evolution Reaction on IrO 2 (110), J. Am. Chem. Soc. 139 (2017) 3473–3479. https://doi.org/10.1021/jacs.6b11932.

[29] I.C. Man, H.Y. Su, F. Calle-Vallejo, H.A. Hansen, J.I. Martínez, N.G. Inoglu, J. Kitchin, T.F. Jaramillo, J.K. Nørskov, J. Rossmeisl, Universality in Oxygen Evolution Electrocatalysis on Oxide Surfaces, ChemCatChem. 3 (2011) 1159–1165. https://doi.org/10.1002/cctc.201000397.

[30] T. Reier, M. Oezaslan, P. Strasser, Electrocatalytic oxygen evolution reaction (OER) on Ru, Ir, and pt catalysts: A comparative study of nanoparticles and bulk materials, ACS Catal. 2 (2012) 1765–1772. https://doi.org/10.1021/cs3003098.

[31] N. Mamaca, E. Mayousse, S. Arrii-Clacens, T.W. Napporn, K. Servat, N. Guillet, K.B. Kokoh, Electrochemical activity of ruthenium and iridium based catalysts for oxygen evolution reaction, Appl. Catal. B Environ. 111–112 (2012) 376–380. https://doi.org/10.1016/j.apcatb.2011.10.020.

[32] J.Y. Kim, J. Choi, H.Y. Kim, E. Hwang, H.-J. Kim, S.H. Ahn, S.-K. Kim, Activity and stability of the oxygen evolution reaction on electrodeposited Ru and its thermal oxides,

Appl. Surf. Sci. 359 (2015) 227–235. https://doi.org/10.1016/j.apsusc.2015.10.082.

[33] T. Reier, Z. Pawolek, S. Cherevko, M. Bruns, T. Jones, D. Teschner, S. Selve, A. Bergmann, H.N. Nong, R. Schlögl, K.J.J. Mayrhofer, P. Strasser, Molecular Insight in Structure and Activity of Highly Efficient, Low-Ir Ir–Ni Oxide Catalysts for Electrochemical Water Splitting (OER), J. Am. Chem. Soc. 137 (2015) 13031–13040. https://doi.org/10.1021/jacs.5b07788.

[34] L. Fu, G. Cheng, W. Luo, Colloidal synthesis of monodisperse trimetallic IrNiFe nanoparticles as highly active bifunctional electrocatalysts for acidic overall water splitting, J. Mater. Chem. A. 5 (2017) 24836–24841. https://doi.org/10.1039/C7TA08982A.

[35] Y. Pi, Q. Shao, P. Wang, J. Guo, X. Huang, General Formation of Monodisperse IrM (M = Ni, Co, Fe) Bimetallic Nanoclusters as Bifunctional Electrocatalysts for Acidic Overall Water Splitting, Adv. Funct. Mater. 27 (2017) 1700886. https://doi.org/10.1002/adfm.201700886.

[36] J. Lim, D. Park, S.S. Jeon, C.-W. Roh, J. Choi, D. Yoon, M. Park, H. Jung, H. Lee, Ultrathin IrO 2 Nanoneedles for Electrochemical Water Oxidation, Adv. Funct. Mater. 28 (2018) 1704796. https://doi.org/10.1002/adfm.201704796.

[37] S.D. Ghadge, O.I. Velikokhatnyi, M.K. Datta, P.M. Shanthi, S. Tan, K. Damodaran, P.N. Kumta, Experimental and Theoretical Validation of High Efficiency and Robust Electrocatalytic Response of One-Dimensional (1D) (Mn,Ir)O 2 :10F Nanorods for the Oxygen Evolution Reaction in PEM-Based Water Electrolysis, ACS Catal. (2019). https://doi.org/10.1021/acscatal.8b02901.

[38] L. Fu, X. Zeng, G. Cheng, W. Luo, IrCo Nanodendrite as an Efficient Bifunctional

Electrocatalyst for Overall Water Splitting under Acidic Conditions, ACS Appl. Mater. Interfaces. 10 (2018) 24993–24998. https://doi.org/10.1021/acsami.8b08717.

[39] W. Hu, S. Chen, Q. Xia, IrO2/Nb–TiO2 electrocatalyst for oxygen evolution reaction in acidic medium, Int. J. Hydrogen Energy. 39 (2014) 6967–6976. https://doi.org/10.1016/j.ijhydene.2014.02.114.

[40] R. Muntean, D.T. Pascal, U. Rost, L. Holtkotte, J. Näther, F. Köster, M. Underberg, T. Hülser, M. Brodmann, Investigation of Iridium Nanoparticles Supported on Sub-stoichiometric Titanium Oxides as Anodic Electrocatalysts in PEM Electrolysis. Part I.: Synthesis and Characterization, Top. Catal. (2019). https://doi.org/10.1007/s11244-019-01164-3.

[41] J. Xu, G. Liu, J. Li, X. Wang, The electrocatalytic properties of an IrO2/SnO2 catalyst using SnO2 as a support and an assisting reagent for the oxygen evolution reaction, Electrochim. Acta. 59 (2012) 105–112. https://doi.org/10.1016/j.electacta.2011.10.044.

[42] L. Solà-Hernández, F. Claudel, F. Maillard, C. Beauger, Doped tin oxide aerogels as oxygen evolution reaction catalyst supports, Int. J. Hydrogen Energy. (2019). https://doi.org/10.1016/j.ijhydene.2019.07.152.

[43] Q. Shi, C. Zhu, H. Zhong, D. Su, N. Li, M.H. Engelhard, H. Xia, Q. Zhang, S. Feng, S.P. Beckman, D. Du, Y. Lin, Nanovoid Incorporated Ir x Cu Metallic Aerogels for Oxygen Evolution Reaction Catalysis, ACS Energy Lett. 3 (2018) 2038–2044. https://doi.org/10.1021/acsenergylett.8b01338.

[44] Y. Zhao, M. Luo, S. Chu, M. Peng, B. Liu, Q. Wu, P. Liu, F.M.F. de Groot, Y. Tan, 3D nanoporous iridium-based alloy microwires for efficient oxygen evolution in acidic media, Nano Energy. 59 (2019) 146–153. https://doi.org/10.1016/j.nanoen.2019.02.020.

[45] Y.T. Kim, P.P. Lopes, S.A. Park, A.Y. Lee, J. Lim, H. Lee, S. Back, Y. Jung, N. Danilovic, V. Stamenkovic, J. Erlebacher, J. Snyder, N.M. Markovic, Balancing activity, stability and conductivity of nanoporous core-shell iridium/iridium oxide oxygen evolution catalysts, Nat. Commun. 8 (2017) 1449. https://doi.org/10.1038/s41467-017-01734-7.

[46] J. Feng, F. Lv, W. Zhang, P. Li, K. Wang, C. Yang, B. Wang, Y. Yang, J. Zhou, F. Lin, G.-C. Wang, S. Guo, Iridium-Based Multimetallic Porous Hollow Nanocrystals for Efficient Overall-Water-Splitting Catalysis, Adv. Mater. 29 (2017) 1703798. https://doi.org/10.1002/adma.201703798.

[47] F. Lv, J. Feng, K. Wang, Z. Dou, W. Zhang, J. Zhou, C. Yang, M. Luo, Y. Yang, Y. Li, P. Gao, S. Guo, Iridium–Tungsten Alloy Nanodendrites as pH-Universal Water-Splitting Electrocatalysts, ACS Cent. Sci. 4 (2018) 1244–1252. https://doi.org/10.1021/acscentsci.8b00426.

[48] A.L. Strickler, R.A. Flores, L.A. King, J.K. Nørskov, M. Bajdich, T.F. Jaramillo, Systematic Investigation of Iridium-Based Bimetallic Thin Film Catalysts for the Oxygen Evolution Reaction in Acidic Media, ACS Appl. Mater. Interfaces. 11 (2019) 34059–34066. https://doi.org/10.1021/acsami.9b13697.

[49] Q. Shi, C. Zhu, D. Du, J. Wang, H. Xia, M.H. Engelhard, S. Feng, Y. Lin, Ultrathin dendritic IrTe nanotubes for an efficient oxygen evolution reaction in a wide pH range, J. Mater. Chem. A. 6 (2018) 8855–8859. https://doi.org/10.1039/C8TA01288A.

[50] J. Joo, H. Jin, A. Oh, B. Kim, J. Lee, H. Baik, S.H. Joo, K. Lee, An IrRu alloy nanocactus on Cu 2−x S@IrS y as a highly efficient bifunctional electrocatalyst toward overall water splitting in acidic electrolytes, J. Mater. Chem. A. 6 (2018) 16130–16138.

https://doi.org/10.1039/C8TA04886J.

[51] S.D. Ghadge, O.I. Velikokhatnyi, M.K. Datta, P.M. Shanthi, S. Tan, K. Damodaran, P.N. Kumta, Experimental and Theoretical Validation of High Efficiency and Robust Electrocatalytic Response of One-Dimensional (1D) (Mn,Ir)O 2 :10F Nanorods for the Oxygen Evolution Reaction in PEM-Based Water Electrolysis, ACS Catal. 9 (2019) 2134–2157. https://doi.org/10.1021/acscatal.8b02901.

[52] S. Chatterjee, C. Griego, J.L. Hart, Y. Li, M.L. Taheri, J. Keith, J.D. Snyder, Free Standing Nanoporous Palladium Alloys as CO Poisoning Tolerant Electrocatalysts for the Electrochemical Reduction of CO2 to Formate, ACS Catal. 9 (2019) 5290–5301. https://doi.org/10.1021/acscatal.9b00330.

[53] Y. Li, T. Polakovic, J. Curtis, S.L. Shumlas, S. Chatterjee, S. Intikhab, D.A. Chareev, O.S. Volkova, A.N. Vasiliev, G. Karapetrov, J. Snyder, Tuning the activity/stability balance of anion doped CoS Se2− dichalcogenides, J. Catal. 366 (2018) 50–60. https://doi.org/10.1016/j.jcat.2018.07.030.

[54] Y. Pi, Q. Shao, X. Zhu, X. Huang, Dynamic Structure Evolution of Composition Segregated Iridium-Nickel Rhombic Dodecahedra toward Efficient Oxygen Evolution Electrocatalysis, ACS Nano. 12 (2018) 7371–7379. https://doi.org/10.1021/acsnano.8b04023.

[55] J. Park, Y.J. Sa, H. Baik, T. Kwon, S.H. Joo, K. Lee, Iridium-Based Multimetallic Nanoframe@Nanoframe Structure: An Efficient and Robust Electrocatalyst toward Oxygen Evolution Reaction, ACS Nano. 11 (2017) 5500–5509. https://doi.org/10.1021/acsnano.7b00233.

[56] H. Jin, Y. Hong, J. Yoon, A. Oh, N.K. Chaudhari, H. Baik, S.H. Joo, K. Lee, Lanthanide

metal-assisted synthesis of rhombic dodecahedral MNi (M = Ir and Pt) nanoframes toward efficient oxygen evolution catalysis, Nano Energy. 42 (2017) 17–25. https://doi.org/10.1016/j.nanoen.2017.10.033.

[57] L.C. Seitz, C.F. Dickens, K. Nishio, Y. Hikita, J. Montoya, A. Doyle, C. Kirk, A. Vojvodic, H.Y. Hwang, J.K. Norskov, T.F. Jaramillo, A highly active and stable IrO x /SrIrO 3 catalyst for the oxygen evolution reaction, Science (80-.). 353 (2016) 1011–1014. https://doi.org/10.1126/science.aaf5050.

[58] X. Tan, J. Shen, N. Semagina, M. Secanell, Decoupling structure-sensitive deactivation mechanisms of Ir/IrOx electrocatalysts toward oxygen evolution reaction, J. Catal. 371 (2019) 57–70. https://doi.org/10.1016/j.jcat.2019.01.018.

[59] M. Li, Z. Zhao, T. Cheng, A. Fortunelli, C.Y. Chen, R. Yu, Q. Zhang, L. Gu, B. V. Merinov, Z. Lin, E. Zhu, T. Yu, Q. Jia, J. Guo, L. Zhang, W.A. Goddard, Y. Huang, X. Duan, Ultrafine jagged platinum nanowires enable ultrahigh mass activity for the oxygen reduction reaction, Science (80-.). 354 (2016) 1414–1419. https://doi.org/10.1126/science.aaf9050.

[60] Y. Li, J.L. Hart, M.L. Taheri, J.D. Snyder, Morphological Instability in Topologically Complex, Three-Dimensional Electrocatalytic Nanostructures, ACS Catal. 7 (2017) 7995–8005. https://doi.org/10.1021/acscatal.7b02398.

[61] Q. Xu, L. Yin, C. Hou, X. Liu, X. Hu, Facile fabrication of nanoporous platinum by alloying–dealloying process and its application in glucose sensing, Sensors Actuators B Chem. 173 (2012) 716–723. https://doi.org/10.1016/j.snb.2012.07.071.

[62] J. Erlebacher, M.J. Aziz, A. Karma, N. Dimitrov, K. Sieradzki, Evolution of nanoporosity in dealloying, Nature. 410 (2001) 450–453. https://doi.org/10.1038/35068529.

[63] J. Snyder, P. Asanithi, A.B. Dalton, J. Erlebacher, Stabilized Nanoporous Metals by Dealloying Ternary Alloy Precursors, Adv. Mater. 20 (2008) 4883–4886. https://doi.org/10.1002/adma.200702760.

[64] Y. Liu, S. Bliznakov, N. Dimitrov, Factors Controlling the Less Noble Metal Retention in Nanoporous Structures Processed by Electrochemical Dealloying, J. Electrochem. Soc. 157 (2010) K168. https://doi.org/10.1149/1.3454753.

[65] J. Snyder, K. Livi, J. Erlebacher, Dealloying silver/gold alloys in neutral silver nitrate solution: Porosity evolution, surface composition, and surface oxides, J. Electrochem. Soc. 155 (2008). https://doi.org/10.1149/1.2940319.

[66] S. Chatterjee, A. Anikin, D. Ghoshal, J.L. Hart, Y. Li, S. Intikhab, D.A. Chareev, O.S. Volkova, A.N. Vasiliev, M.L. Taheri, N. Koratkar, G. Karapetrov, J. Snyder, Nanoporous metals from thermal decomposition of transition metal dichalcogenides, Acta Mater. 184 (2020) 79–85. https://doi.org/10.1016/j.actamat.2019.11.018.

[67] Z. Zhang, Y. Wang, Z. Qi, W. Zhang, J. Qin, J. Frenzel, Generalized Fabrication of Nanoporous Metals (Au, Pd, Pt, Ag, and Cu) through Chemical Dealloying, J. Phys. Chem. C. 113 (2009) 12629–12636. https://doi.org/10.1021/jp811445a.

[68] P. Mani, R. Srivastava, P. Strasser, Dealloyed binary PtM3 (M=Cu, Co, Ni) and ternary PtNi3M (M=Cu, Co, Fe, Cr) electrocatalysts for the oxygen reduction reaction: Performance in polymer electrolyte membrane fuel cells, J. Power Sources. 196 (2011) 666–673. https://doi.org/10.1016/j.jpowsour.2010.07.047.

[69] S.J. Freakley, J. Ruiz-Esquius, D.J. Morgan, The X-ray photoelectron spectra of Ir, IrO 2 and IrCl 3 revisited, Surf. Interface Anal. 49 (2017) 794–799. https://doi.org/10.1002/sia.6225.

[70] J. Erlebacher, An Atomistic Description of Dealloying, J. Electrochem. Soc. 151 (2004) C614–C626. https://doi.org/10.1149/1.1784820.

[71] E. Detsi, M. Van De Schootbrugge, S. Punzhin, P.R. Onck, J.T.M. De Hosson, On tuning the morphology of nanoporous gold, Scr. Mater. 64 (2011) 319–322. https://doi.org/10.1016/j.scriptamat.2010.10.023.

[72] C.Q. Sun, Y. Wang, B.K. Tay, S. Li, H. Huang, Y.B. Zhang, Correlation between the melting point of a nanosolid and the cohesive energy of a surface atom, J. Phys. Chem. B. 106 (2002) 10701–10705. https://doi.org/10.1021/jp025868l.

[73] F.U. Renner, A. Stierle, H. Dosch, D.M. Kolb, J. Zegenhagen, The influence of chloride on the initial anodic dissolution of Cu3Au(111), Electrochem. Commun. 9 (2007) 1639–1642. https://doi.org/10.1016/j.elecom.2007.03.001.

[74] G.N. Ankah, A. Pareek, S. Cherevko, A.A. Topalov, M. Rohwerder, F.U. Renner, The influence of halides on the initial selective dissolution of Cu3Au (111), Electrochim. Acta. 85 (2012) 384–392. https://doi.org/10.1016/j.electacta.2012.08.059.

[75] D.K. Pattadar, F.P. Zamborini, Halide-Dependent Dealloying of Cu x /Au y Core/Shell Nanoparticles for Composition Analysis by Anodic Stripping Voltammetry, J. Phys. Chem. C. 123 (2019) 9496–9505. https://doi.org/10.1021/acs.jpcc.8b12174.

[76] Z. Zhang, C. Zhang, J. Sun, T. Kou, Influence of anion species on electrochemical dealloying of single-phase Al2Au alloy in sodium halide solutions, RSC Adv. 2 (2012) 4481. https://doi.org/10.1039/c2ra20087b.

[77] D. V. Pugh, A. Dursun, S.G. Corcoran, Electrochemical and Morphological Characterization of Pt–Cu Dealloying, J. Electrochem. Soc. 152 (2005) B455. https://doi.org/10.1149/1.2048140.

[78] A.S.M. Handbook, Alloy Phase Diagram, vol. 3, 1992. https://doi.org/10.1007/BF02869318.

[79] Q. Chen, Z. Cao, G. Du, Q. Kuang, J. Huang, Z. Xie, L. Zheng, Excavated octahedral Pt-Co alloy nanocrystals built with ultrathin nanosheets as superior multifunctional electrocatalysts for energy conversion applications, Nano Energy. 39 (2017) 582–589. https://doi.org/10.1016/j.nanoen.2017.07.041.

[80] L. Chen, H. Guo, T. Fujita, A. Hirata, W. Zhang, A. Inoue, M. Chen, Nanoporous PdNi Bimetallic Catalyst with Enhanced Electrocatalytic Performances for Electro-oxidation and Oxygen Reduction Reactions, Adv. Funct. Mater. 21 (2011) 4364–4370. https://doi.org/10.1002/adfm.201101227.

[81] W. Du, Q. Wang, D. Saxner, N.A. Deskins, D. Su, J.E. Krzanowski, A.I. Frenkel, X. Teng, Highly Active Iridium/Iridium–Tin/Tin Oxide Heterogeneous Nanoparticles as Alternative Electrocatalysts for the Ethanol Oxidation Reaction, J. Am. Chem. Soc. 133 (2011) 15172–15183. https://doi.org/10.1021/ja205649z.

[82] H.G. Sanchez Casalongue, M.L. Ng, S. Kaya, D. Friebel, H. Ogasawara, A. Nilsson, In Situ Observation of Surface Species on Iridium Oxide Nanoparticles during the Oxygen Evolution Reaction, Angew. Chemie Int. Ed. 53 (2014) 7169–7172. https://doi.org/10.1002/anie.201402311.

[83] S. Jung, C.C.L. McCrory, I.M. Ferrer, J.C. Peters, T.F. Jaramillo, Benchmarking nanoparticulate metal oxide electrocatalysts for the alkaline water oxidation reaction, J. Mater. Chem. A. 4 (2016) 3068–3076. https://doi.org/10.1039/C5TA07586F.

[84] C. Wei, R.R. Rao, J. Peng, B. Huang, I.E.L. Stephens, M. Risch, Z.J. Xu, Y. Shao-Horn, Recommended Practices and Benchmark Activity for Hydrogen and Oxygen

Electrocatalysis in Water Splitting and Fuel Cells, Adv. Mater. 31 (2019) 1806296. https://doi.org/10.1002/adma.201806296.

[85] Y. Yoon, B. Yan, Y. Surendranath, Suppressing Ion Transfer Enables Versatile Measurements of Electrochemical Surface Area for Intrinsic Activity Comparisons, J. Am. Chem. Soc. 140 (2018) 2397–2400. https://doi.org/10.1021/jacs.7b10966.

[86] E. Burke, L., O'Sullivan, Oxygen gas evolution on hydrous oxides - An example of three-dimensional electrocatalysis?, J. Electroanal. Chem. Interfacial Electrochem. 117 (1981) 155–160.

[87] R.L. Doyle, I.J. Godwin, M.P. Brandon, M.E.G. Lyons, Redox and electrochemical water splitting catalytic properties of hydrated metal oxide modified electrodes, Phys. Chem. Chem. Phys. 15 (2013) 13737–13783. https://doi.org/10.1039/c3cp51213d.

[88] C. Wei, S. Sun, D. Mandler, X. Wang, S.Z. Qiao, Z.J. Xu, Approaches for measuring the surface areas of metal oxide electrocatalysts for determining their intrinsic electrocatalytic activity, Chem. Soc. Rev. 48 (2019) 2518–2534. https://doi.org/10.1039/c8cs00848e.

[89] M.B. Stevens, L.J. Enman, A.S. Batchellor, M.R. Cosby, A.E. Vise, C.D.M. Trang, S.W. Boettcher, Measurement Techniques for the Study of Thin Film Heterogeneous Water Oxidation Electrocatalysts, Chem. Mater. 29 (2017) 120–140. https://doi.org/10.1021/acs.chemmater.6b02796.

[90] C.C.L. McCrory, S. Jung, J.C. Peters, T.F. Jaramillo, Benchmarking Heterogeneous Electrocatalysts for the Oxygen Evolution Reaction, J. Am. Chem. Soc. 135 (2013) 16977–16987. https://doi.org/10.1021/ja407115p.

[91] B.M. Tackett, W. Sheng, S. Kattel, S. Yao, B. Yan, K.A. Kuttiyiel, Q. Wu, J.G. Chen, Reducing Iridium Loading in Oxygen Evolution Reaction Electrocatalysts Using Core–

Shell Particles with Nitride Cores, ACS Catal. 8 (2018) 2615–2621. https://doi.org/10.1021/acscatal.7b04410.

[92] T. Hepel, Irreversible Voltammetric Behavior of the (100) IrO[sub 2] Single-Crystal Electrodes in Sulfuric Acid Medium, J. Electrochem. Soc. 132 (1985) 2385. https://doi.org/10.1149/1.2113583.

[93] H.-S. Oh, H.N. Nong, T. Reier, A. Bergmann, M. Gliech, J. Ferreira de Araújo, E. Willinger, R. Schlögl, D. Teschner, P. Strasser, Electrochemical Catalyst–Support Effects and Their Stabilizing Role for IrO x Nanoparticle Catalysts during the Oxygen Evolution Reaction, J. Am. Chem. Soc. 138 (2016) 12552–12563. https://doi.org/10.1021/jacs.6b07199.

[94] D.F. Abbott, D. Lebedev, K. Waltar, M. Povia, M. Nachtegaal, E. Fabbri, C. Copéret, T.J. Schmidt, Iridium Oxide for the Oxygen Evolution Reaction: Correlation between Particle Size, Morphology, and the Surface Hydroxo Layer from Operando XAS, Chem. Mater. 28 (2016) 6591–6604. https://doi.org/10.1021/acs.chemmater.6b02625.

[95] H. Yu, N. Danilovic, Y. Wang, W. Willis, A. Poozhikunnath, L. Bonville, C. Capuano, K. Ayers, R. Maric, Nano-size IrOx catalyst of high activity and stability in PEM water electrolyzer with ultra-low iridium loading, Appl. Catal. B Environ. 239 (2018) 133–146. https://doi.org/10.1016/j.apcatb.2018.07.064.

[96] C. Rozain, E. Mayousse, N. Guillet, P. Millet, Influence of iridium oxide loadings on the performance of PEM water electrolysis cells: Part I–Pure IrO 2 -based anodes, Appl. Catal. B Environ. 182 (2016) 153–160. https://doi.org/10.1016/j.apcatb.2015.09.013.

[97] A.R.C. Bredar, A.L. Chown, A.R. Burton, B.H. Farnum, Electrochemical Impedance Spectroscopy of Metal Oxide Electrodes for Energy Applications, ACS Appl. Energy

Mater. 3 (2020) 66–98. https://doi.org/10.1021/acsaem.9b01965.

[98] S.M. Alia, B. Rasimick, C. Ngo, K.C. Neyerlin, S.S. Kocha, S. Pylypenko, H. Xu, B.S. Pivovar, Activity and Durability of Iridium Nanoparticles in the Oxygen Evolution Reaction, J. Electrochem. Soc. 163 (2016) F3105–F3112. https://doi.org/10.1149/2.0151611jes.

[99] Z. Yan, Y. Zhao, Z. Zhang, G. Li, H. Li, J. Wang, Z. Feng, M. Tang, X. Yuan, R. Zhang, Y. Du, A study on the performance of IrO2–Ta2O5 coated anodes with surface treated Ti substrates, Electrochim. Acta. 157 (2015) 345–350. https://doi.org/10.1016/j.electacta.2015.01.005.

[100] F. Claudel, L. Dubau, G. Berthomé, L. Sola-Hernandez, C. Beauger, L. Piccolo, F. Maillard, Degradation Mechanisms of Oxygen Evolution Reaction Electrocatalysts: A Combined Identical-Location Transmission Electron Microscopy and X-ray Photoelectron Spectroscopy Study, ACS Catal. 9 (2019) 4688–4698. https://doi.org/10.1021/acscatal.9b00280.

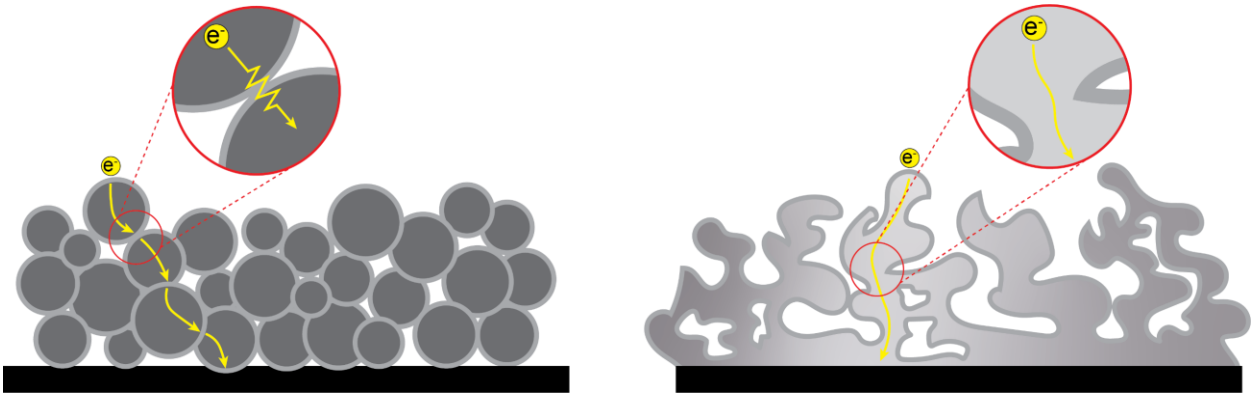

Figure 1: Schematic representation of (left) a traditional IrO_x anode catalyst layer containing a high density of oxide-oxide interfaces that yield a low in-plane and through-plane conductivity, negatively impacting OER high current density performance; (right) np-Ir electrode characterized by a thin amorphous oxide surface coating with a bicontinuous metallic backbone that results in high in-plane and through-plane conductivity.

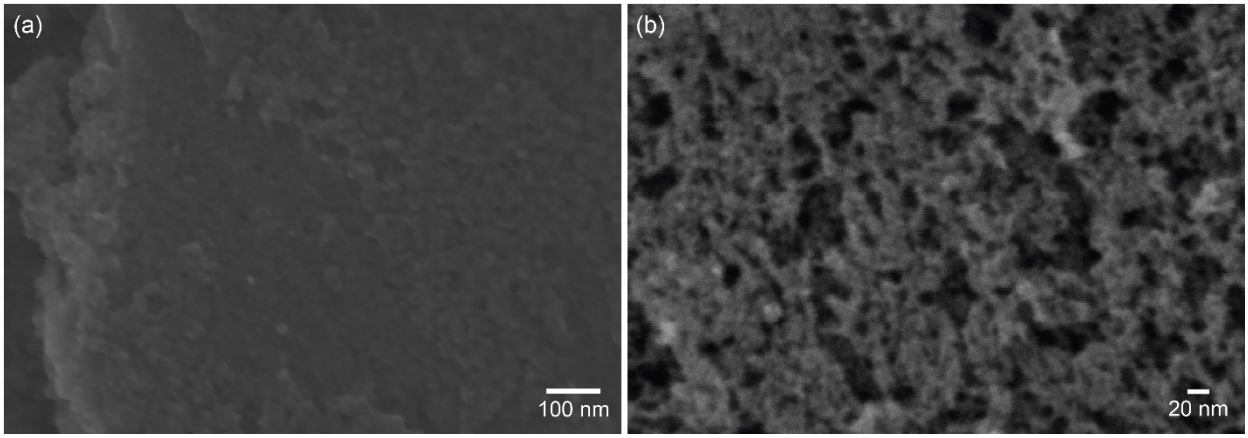

Figure 2: SEM of post dealloyed $Ni_{85}Ir_{15}$ alloys obtained through potentiodynamic dealloying in (a) 1 M H_2SO_4 and (b) 1 M H_2SO_4 + 0.1 M HCl.

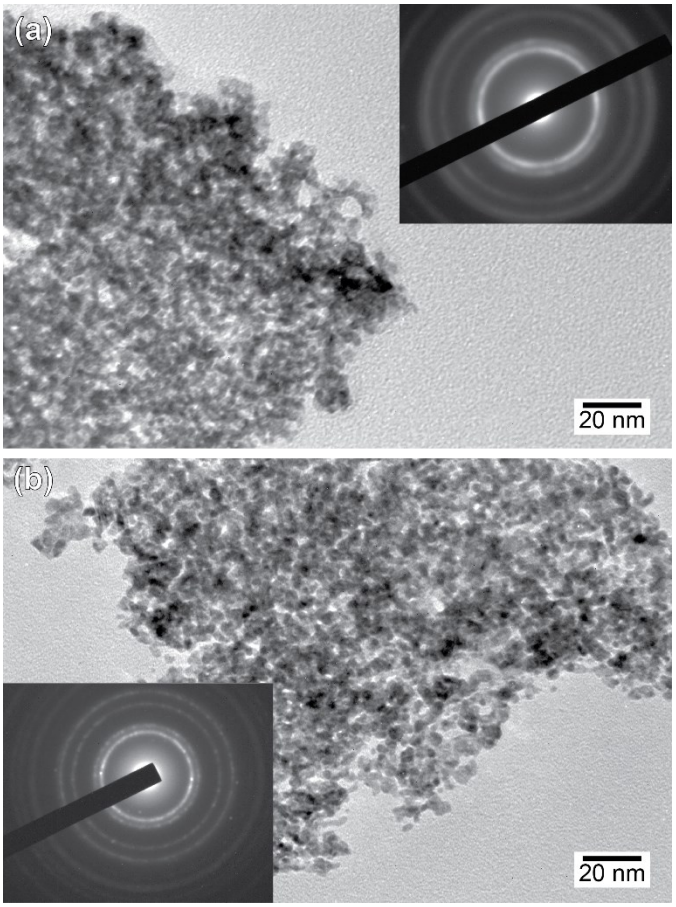

Figure 3: TEMs of (a) np-Ir and (b) np-IrCr formed through electrochemical dealloying in 1 M H_2SO_4 + 0.1 M HCl. Insets are the SAED patterns.

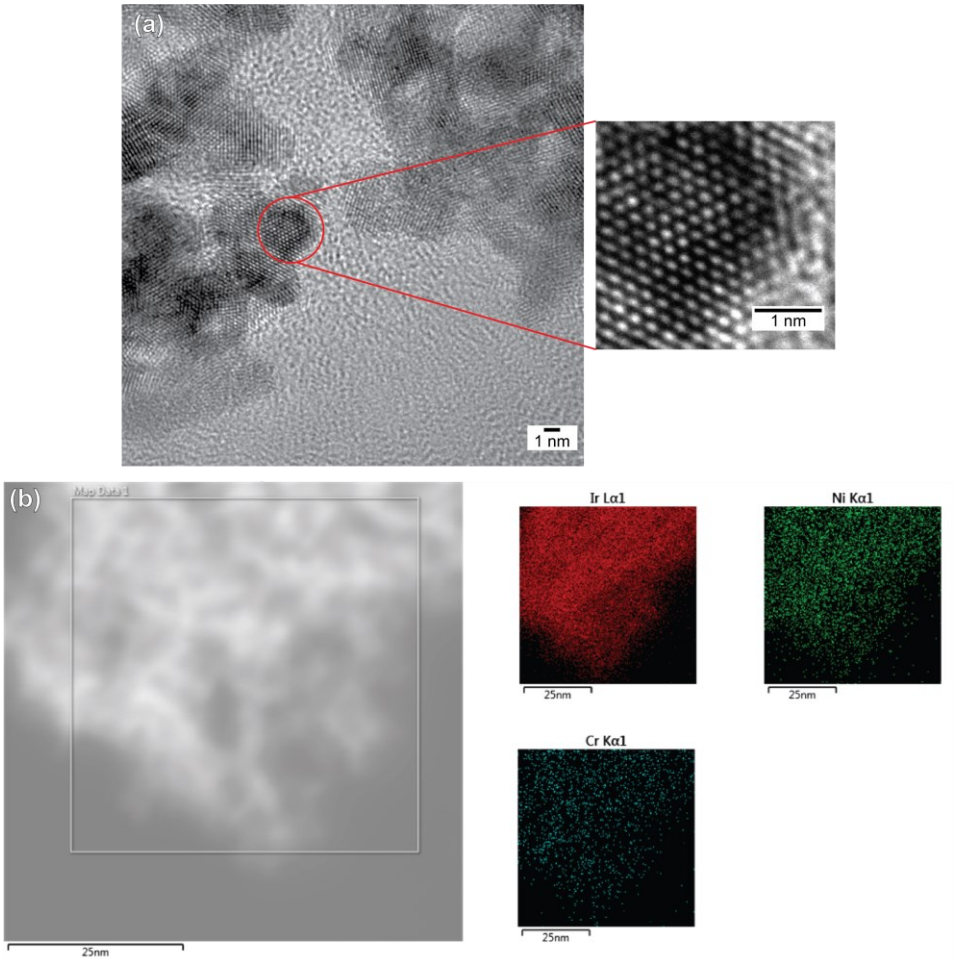

Figure 4: (a) HRTEM micrograph of np-IrCr with high magnification inset. (b) EDS elemental mapping (HAADF STEM mode) of np-IrCr.

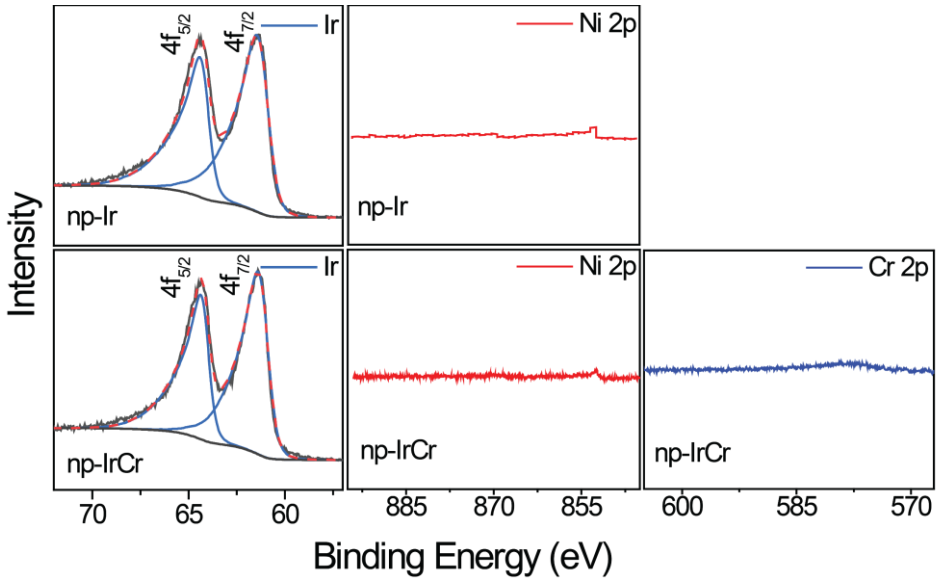

Figure 5: XPS spectra of electrochemically dealloyed np-Ir and np-IrCr (potentiodynamic dealloying in 1 M H_2SO_4 + 0.1 M HCl).

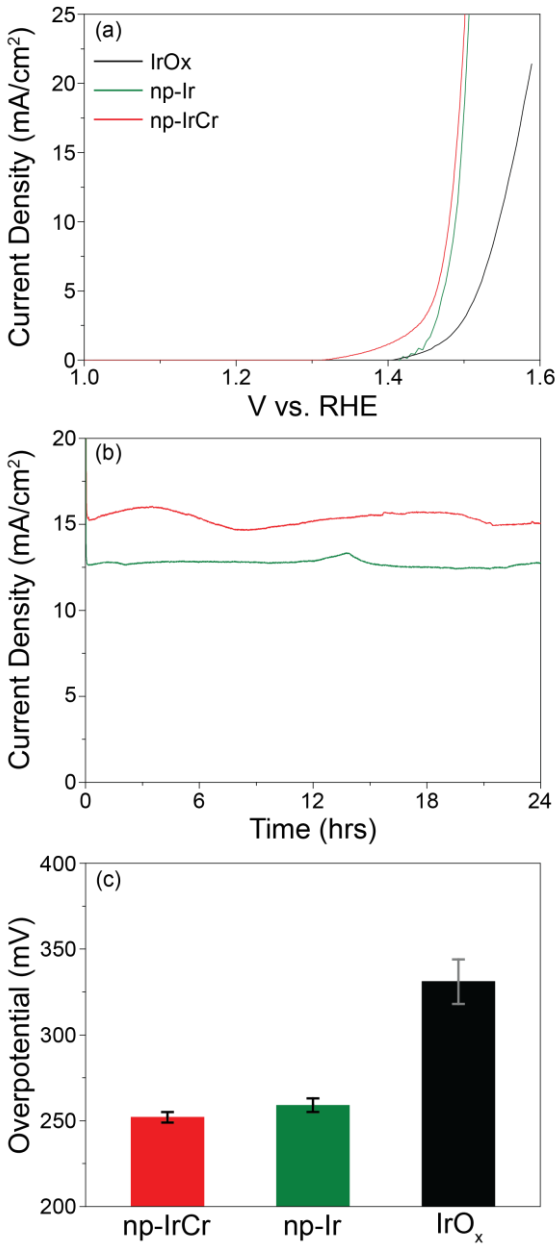

Figure 6: (a) OER polarization curves (current normalized by electrode geometric area) for IrO_x (black), np-Ir (green) and np-IrCr (red) in Ar purged 0.1 M $HClO_4$ (10 mV/s sweep rate). (b) Constant potential (1.51 V vs. RHE) OER electrolysis for np-Ir (green) and np-IrCr (red). Current here is normalized by the geometric area of the electrodes. (c) OER overpotentials at 10 mA/cm^2 (electrode geometric area normalized current densities).

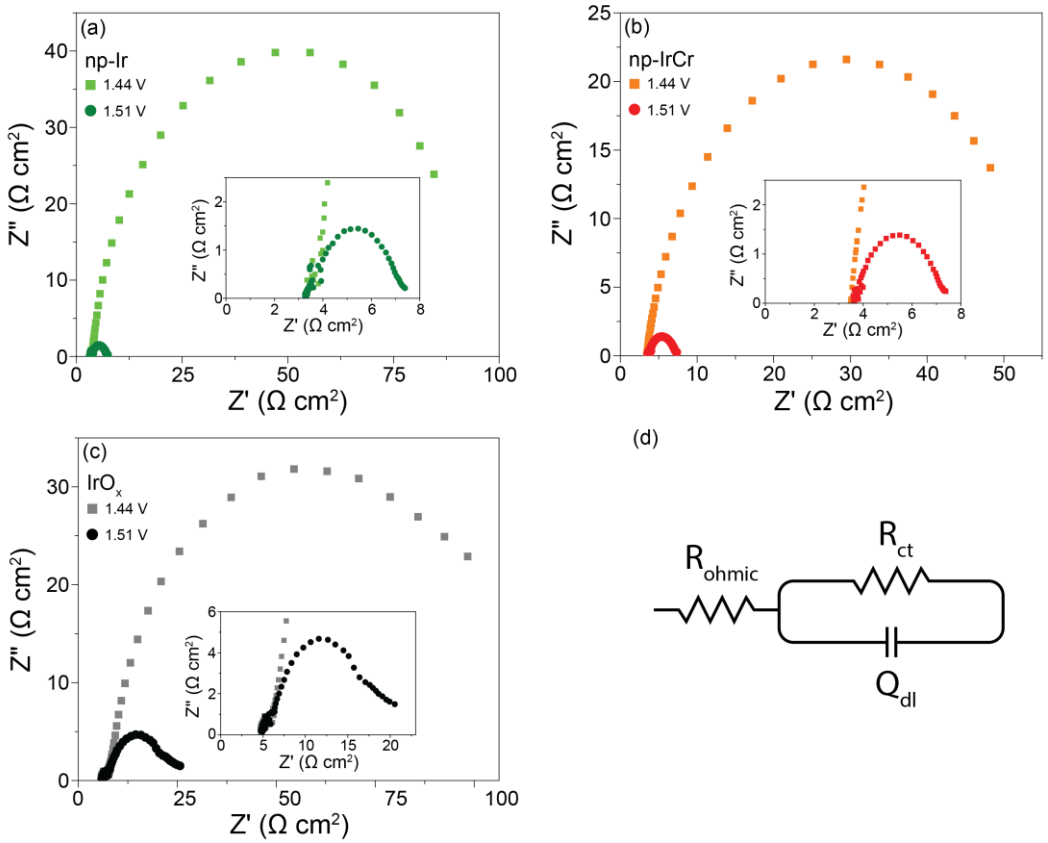

Figure 7: Nyquist plots at 1.44 and 1.51 V vs. RHE in 0.1 M $HClO_4$ on (a) np-Ir, (b) np-IrCr, and (c) IrO_x. (d) Equivalent circuit diagram used to determine ohmic and charge transfer resistances.